UCLA
UCLA Electronic Theses and Dissertations

Title

Effect of Tides and Currents on UAV-Based Detection of Giant Kelp Canopy

Permalink

https://escholarship.org/uc/item/0tn1p1p6

Author

Cavanaugh, Katherine C

Publication Date

2020

Peer reviewed|Thesis/dissertation

UNIVERSITY OF CALIFORNIA

Los Angeles

Effect of Tides and Currents on UAV-Based

Detection of Giant Kelp Canopy

A thesis submitted in partial satisfaction

of the requirements for the degree of Master of

Arts in Geography

by

Katherine C. Cavanaugh

2020

ABSTRACT OF THESIS

Effect of Tides and Currents on UAV-Based

Detection of Giant Kelp Canopy

by

Katherine C. Cavanaugh

Master of Arts in Geography

University of California, Los Angeles, 2020

Professor Kyle C. Cavanaugh, Chair

Satellite and aerial imagery have been used extensively for mapping the abundance and distribution of giant kelp (*Macrocystis pyrifera*) in southern California. While tides and currents have been shown to affect the amount of floating kelp canopy on the water surface, there have been no quantifications of how these processes can bias remotely sensed kelp estimates in this region. We used unmanned aerial vehicles (UAVs) to map fine-scale changes in canopy area due to tidal height and current speed at both Palos Verdes, CA and Santa Barbara, CA. Additionally, we collected a biweekly time series of kelp canopy area in Palos Verdes over the course of a year to monitor fine-scale, intra-seasonal changes in canopy coverage. Our automated method for detecting kelp canopy in color and multispectral UAV imagery was highly accurate (over 84% and 98%, respectively) in classifying exemplary kelp and water pixels across a range of weather, ocean, and illumination conditions. Increases in tidal height of 1 m reduced the amount of floating kelp

canopy by 15% to 32%. Current speeds are generally low in southern California and had no statistically significant effect on apparent bed size. However, increases in current speeds of 0.1 m/s reduced the amount of floating kelp canopy by over 31%. Tidal height and current speed can introduce significant variability to estimates of kelp abundance, but the magnitude of this variability is region specific. The biweekly time series displayed intra-annual variability typical of giant kelp, with a relatively gradual decline in kelp canopy in late summer corresponding with high sea surface temperatures, a rapid decline in the winter associated with wave disturbance, and a gradual recovery in the spring of the following year. The time series was also able to capture intra-seasonal changes in kelp canopy area that would have gone undetected in an annual or quarterly dataset, namely an increase in area to about half of the maximum in the late fall before wave events began.

The thesis of Katherine C. Cavanaugh is approved.

Thomas Welch Gillespie

Yongwei Sheng

Kyle C. Cavanaugh, Committee Chair

University of California, Los Angeles

2020

TABLE OF CONTENTS

LIST OF FIGURES

LIST OF TABLES

ACKNOWLEDGEMENTS

1. Introduction

Giant kelp (*Macrocystis pyrifera*) serves as the structural and nutritional foundation for globally distributed and highly productive nearshore ecosystems (Dugan et al., 2003; Graham et al., 2007; Miller et al., 2018). Giant kelp forests offer great societal and economic value through the support of fisheries, recreation, a wide range of products including cosmetics, food, and fertilizer, and the potential for biofuel production (Gentry et al., 2017, 2019). Accordingly, monitoring the abundance and distribution of this valuable resource is particularly important in the face of global climate change, as marine ecosystems are especially susceptible to the effects of climatic disturbances (Harley et al., 2006).

Fixed to subtidal, rocky reefs with a holdfast, giant kelp fronds vertically extend towards the sea surface to form dense, floating canopies, which are easily visible from above. The use of satellite imagery has shown great potential for monitoring kelp populations, as floating kelp canopies are visible with moderate resolution (10 to 30 m) spaceborne sensors (Bell et al., 2020; Bell, Cavanaugh, Reed, et al., 2015; Cavanaugh et al., 2011; Mora-Soto et al., 2020). Repeated global measurements provide a comprehensive view of changes in kelp canopy area through time, enabling the purported roles of seasonal (e.g. wave disturbance and nutrient availability) to decadal scale (e.g. the El Niño-Southern Oscillation (ENSO) and the North Pacific Gyre Oscillation (NPGO)) drivers to be evaluated across a wide range of spatial scales. Satellites with moderate resolution can be used to accurately estimate the biomass of continuous kelp canopies ranging on the order of tens of meters to hundreds of kilometers in size (Cavanaugh et al., 2011), yet are unable to detect sparse stands of kelp that cover less than 15% of a pixel (Hamilton et al., 2020). Additionally, shallow kelp communities are often difficult to differentiate from land, especially when pixels contain a mixture of land, water, and kelp (Bell et al., 2020; Hamilton et al., 2020; Schroeder et al., 2019). These issues limit the suitability of moderate resolution

1

satellite imagery for monitoring giant kelp habitat in regions where kelp beds are small, sparse and/or found close to the shoreline (e.g. British Colombia; Nijland et al., 2019).

Unmanned aerial vehicles (UAVs) present a low-cost, versatile solution to the challenges and limitations associated with using satellite imagery to study small or sparse kelp beds. Offering spatial resolutions on the order of centimeters, UAVs not only provide the fine resolution necessary to monitor environmental processes on fine spatial scales, but they also present the flexibility for high temporal resolutions (Whitehead et al., 2014; Whitehead & Hugenholtz, 2014). Additionally, sensor systems with varying spectral capabilities have been developed for UAV platforms, ranging from digital color cameras, containing red, green, and blue channels (RGB) to hyperspectral (Whitehead & Hugenholtz, 2014). While emergent giant kelp canopy prominently reflects in the near infrared (NIR), water has a high absorption (Jensen et al., 1980; Schroeder et al., 2019). As a result, NIR reflectance decreases as kelp fronds submerge, making this portion of the spectrum useful for detecting canopy coverage and mapping fine-scale changes through time (Cavanaugh et al., 2010).

Tidal height and surface currents introduce complexity into aerial estimates of kelp canopy area (Britton-Simmons et al., 2008). The amount of kelp exposed on the water surface periodically fluctuates with incoming and outgoing tides. Portions of the canopy submerge and reemerge as tidal height increases and decreases, and at high-tide, deeply submerged individuals become undetectable with aerial and satellite-based sensors. Similarly, strong currents can temporarily immerse floating canopies, changing the shape and coverage of the forest when viewed from above.

In southern California, satellite and aerial imagery have been used extensively for monitoring the drivers of giant kelp biomass dynamics, kelp physiological condition, and synchrony and metapopulation dynamics (Jensen et al., 1980; Deysher 1993; Stekoll et al., 2006;

Cavanaugh et al., 2011; 2013; 2014; 2019; Bell et al., 2015a,b; 2020; Castorani et al., 2015; 2017). Despite this widespread use, it is unclear how tidal height and surface currents impact apparent bed size in this region. Britton-Simmons et al. (2008) demonstrated a significant impact of tides and currents on bull kelp (*Nereocystis luetkeana*) canopy using oblique-angle, shore-based photography. However, there are limitations with estimating area from oblique-angle imagery, and bull kelp has a different morphology than giant kelp.

Here, we aim to quantify the influence of tides and currents on floating giant kelp canopy in southern California using UAVs. UAV imagery has been successfully implemented in the detection and mapping of both floating and submerged seaweed communities, yet sun glint, crashing waves, shadows, and spectral noise have made automated classification schemes problematic, necessitating manual image classifications (Kellaris et al., 2019; Taddia & Russo, 2019; Thomsen et al., 2019). As a result, another goal of this work is to develop an automated canopy detection algorithm that can be applied consistently to UAV imagery collected across varying conditions. Last, using this automated method, we introduce a new data set created from multispectral UAV imagery which allows for the local scale assessment of giant kelp canopy area at 10 cm resolution every two weeks for one year while controlling for tides.

2. Methods

2.1 Field Data Collection

Our study area included two kelp forests located on the southern California coast: Arroyo Quemado (34° 28.127′ N, 120° 07.285′ W) west of Santa Barbara, and Honeymoon Cove (33° 45.906′ N, 118° 25.392′ W) at Palos Verdes (Fig. 1). Both kelp forests experience tidal fluctuations ranging from ~ -0.55 m to 2.2 m.
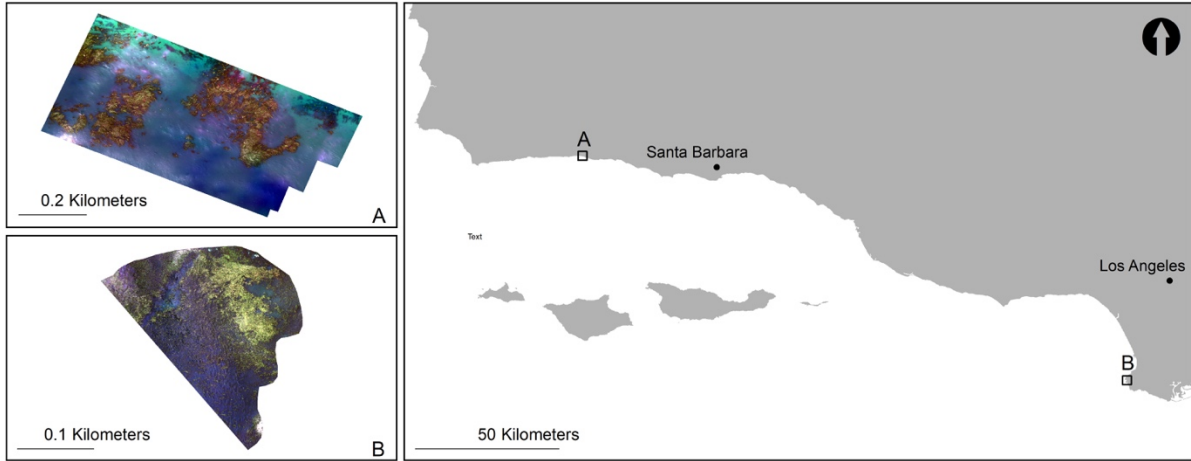
Fig. 1. Santa Barbara, California study site: Arroyo Quemado (A) and Palos Verdes, California study site: Honeymoon Cove (B).

We conducted flights throughout the tidal range (hereafter referred to as tidal surveys) on 2 January 2018 at Arroyo Quemado (-0.52 m to 2.15 m) and on 9 July 2018 (0.64 m to 1.96 m) and 18 July 2018 (0.25 m to 1.56 m) at Honeymoon Cove to capture the tidal responses of kelp beds with different structural properties. The Arroyo Quemado kelp forest is located offshore of an open coast, and we sampled one discrete stand within the forest located ~ 400 m from the shoreline (surveyed a total area of 0.29 km^2). We were able to completely capture the stand in our imagery. The Honeymoon Cove kelp forest extends throughout a sheltered cove, with thicker stands of kelp fringing the coastline and sparser stands of kelp covering the rest of the cove. We only conducted flights within the cove, but the kelp forest continuously extended past the section we surveyed (surveyed a total area of 0.25 km^2). For each tidal survey, we performed hourly flights across the tidal amplitude (approximately six hours). Wind speeds were less than 8 km/h during all tidal survey flights.

Current measurements were not available at Honeymoon Cove, but we performed replicate tidal flights 9 days apart for comparison. We conducted a separate set of surveys at Arroyo Quemado to isolate the effect of currents on apparent kelp bed site (hereafter referred to

as current survey). These consisted of one flight per day at the bottom of low tide across a 5-day span (26 June 2019 to 30 June 2019) with varying wind speeds.

We used a MicaSense RedEdge sensor mounted on a DJI Matrice 100 quadcopter to survey the kelp bed at Honeymoon Cove. The RedEdge simultaneously captures data in five spectral channels, the blue (475 nm), green (560 nm), red (668 nm), red-edge (717 nm), and NIR (840 nm). Sun angle and illumination conditions varied temporally across each survey, and while the RedEdge was equipped with a downwelling light sensor (DLS), we omitted DLS data in image processing to reduce bias introduced by DLS tilting during the flight (Hakala et al., 2018). To calibrate reflectance for each flight, we imaged a spectral calibration panel with known reflectance before and after each flight. We set the along-track overlap between consecutive images to 80% and the side-track overlap between consecutive flight lines to a minimum of 75%. Sun glint distorted the reflectance of pixels in the middle and edges of images taken when the sun was at or close to zenith. To increase pixel coverage unaffected by sun glint, we increased the side-track overlap to 85% during these flights. We used a MicaSense Altum sensor mounted on a DJI Matrice 200 quadcopter to survey the kelp bed at Arroyo Quemado. The Altum simultaneously captures data in the same five channels as the RedEdge. We kept all other settings consistent to those used with the RedEdge sensor.

A moored CTD and Acoustic Doppler Current Profiler (ADCP) from the Santa Barbara Coastal Long Term Ecological Research (SBC LTER) program (http://sbc.lternet.edu) were located within the Arroyo Quemado kelp forest, allowing for simultaneous *in situ* depth and current measurement comparisons with each Arroyo Quemado flight. These data included north velocity, east velocity, and water depth, which were provided in 20-minute intervals. Velocity data were collected at 16 different heights in the water column, from 2.5 m to 17.5 m from the bottom. We used measurements from 12.5 m readings for this study, as measurements taken

5

above 12.5 m from the bottom often yielded no data values at low tide. We linearly interpolated both depth and current measurements to 1-minute intervals to match the tidal height and current speed at the time each kelp forest was imaged. We used NOAA/NOS/CO-OPS 1-minute tidal measurements (https://tidesandcurrents.noaa.gov/1mindata.html) from Station 9410660 for simultaneous *in situ* depth measurement comparisons with each Honeymoon Cove flight.

2.2 UAV Image Data Processing

Before analyzing the UAV images, we converted raw pixel values from digital numbers (DN) to reflectance using the recommended MicaSense processing steps (https://github.com/micasense/imageprocessing). We applied a dark pixel correction to reduce sensor noise, calculated an imager specific radiometric calibration function to account for radiometric inaccuracies, removed vignette effects from image corners, and divided each pixel by image gain, exposure time, and a sensor-specific calibration coefficient (all imager and sensor specific calibrations were provided within the MicaSense GitHub). For each band, we extracted and averaged the pixels within the inner 75% of reflectance panel images captured before and after each flight to account for any illumination changes from launch to landing. The respective panels for the RedEdge and Altum have a known reflectance for each band, which we used to convert DN to reflectance.

Pixels altered by sun glint and crashing waves introduce distortion into individual images, as these pixels are inconsistent across space and time, making image mosaicking difficult. To reduce distortion, we masked these pixels from each band of pre-mosaicked reflectance images using gray-level co-occurrence matrices (GLCM), which have been successful in a variety of remote sensing-based classifications (Changhui et al., 2013; X. Huang et al., 2014; Zheng et al., 2018). GLCMs yield textural features from images by calculating the

spatial distribution of the gray-level variations of individual band values (Haralick et al., 1973). The function *graycomatrix* in MATLAB 2018a creates a GLCM by describing pixel spatial dependency, or the frequency at which a pixel with value *i* occurs adjacent to a pixel with value *j* (MATLAB 2018a). Because sun glint was most prominent in the blue band of RedEdge and Altum images, we ran *graycomatrix* on the blue band of each image. We used the brightest pixel grouping within each matrix to mask glint and wave pixels for all images containing 100% water to minimize accidental masking of land and coastal pixels. We put a 5-pixel buffer around any pixels classified as glint and exported a unique mask for each individual UAV image (Fig. 2). We mosaicked reflectance images into orthomosaics using the photogrammetric software Agisoft Photoscan Pro and exported each resulting flight as a GeoTiff (Agisoft, St. Petersburg, Russia). Masks can be imported directly into Photoscan Pro, which ignores masked values when finding tie points for photogrammetric stitching. To account for error in measurements of the UAV's onboard GPS, we manually georeferenced each GeoTiff to an arbitrarily selected base image using ten coordinates located along the shoreline of each site. Once images were georeferenced, they were resampled to 10 cm x 10 cm, and all land and coastal pixels within 10 meters of the low-tide line were removed.
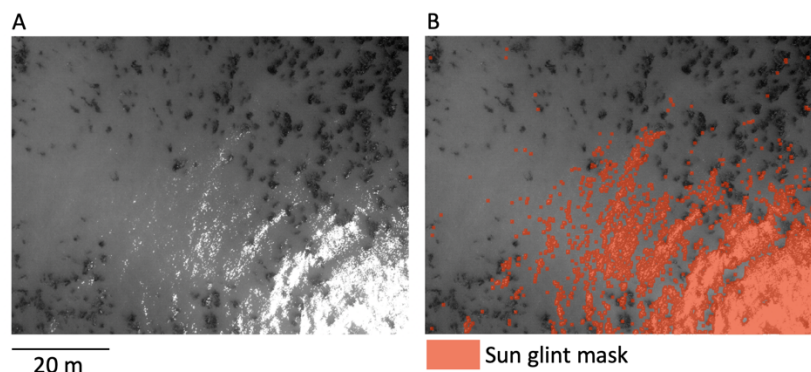

Fig. 2. Unprocessed, grayscale UAV image (A) and corresponding sun glint mask (B). All reflectance pixels found within the sun glint mask were removed during photogrammetric processing to improve mosaicking success.

2.3 UAV-Based Kelp Area Detection

We compared twenty vegetation indices to determine which was best at separating kelp from water in UAV imagery. These included both previously published indices as well as simple additive and multiplicative band combinations. Ten indices were restricted to RGB wavelengths, and ten indices included either the red-edge or NIR band (Table 1). To compare the performance of various vegetation indices in detecting kelp canopy, we manually identified kelp and water pixels across 10 dates from the Honeymoon Cove time series with varying sun angles, wind speeds, wave conditions, water clarity, and kelp health to cover a wide range of conditions experienced in the field. The number of identified kelp and water pixels varied from image to image, and to keep samples consistent, we randomly selected 500 pixels from each class within each image for a total of 5,000 pixels per class. We then used two parametric separability measures, the transformed divergence (TD) separability measure (Equation 1, Equation 2) and the Jeffries-Matusita distance (JM; Equation 3, Equation 4), to assess the ability of each index to differentiate kelp from water. JM and TD are both statistical mechanisms for testing the ability to distinguish two classes. Each is bound between 0 and 2, with 0 being no separability between classes and 2 being complete class separability as:

$$Divergence\ (D) = \frac{1}{2}tr[(C_1 - C_2)(C_1^{-1} - C_2^{-1})] + \frac{1}{2}tr[(C_1^{-1} - C_2^{-1})(\mu_1-\mu_2)(\mu_1-\mu_2)^T] \quad (1)$$

$$TD = 2\left[1 - \exp\left(-\frac{D}{8}\right)\right] \quad (2)$$

$$Bhattacharyya\ distance\ (BD) = \frac{1}{8}(\mu_2-\mu_1)^T\left[\frac{C_1+C_2}{2}\right]^{-1}(\mu_2-\mu_1) + \frac{1}{2}\ln\frac{\left|\frac{C_1+C_2}{2}\right|}{\sqrt{|C_1||C_2|}} \quad (3)$$

$$JM = \sqrt{2[1 - \exp(-BD)]} \quad (4)$$

where C_1 and C_2 are the covariance matrices of class 1 and class 2, μ_1 and μ_2 are the mean

vectors of class 1 and class 2, *tr* is the matrix trace function, and *T* is the matrix transposition function. JM and TD are the transformed divergence and Jeffries-Matusita distances between class 1 and class 2, respectively (Jensen 1996; H. Huang et al. 2016).

Because JM and TD are only indicative of separability in cases of normality, we used the Shapiro-Wilk Normality test to determine whether the kelp and water pixel samples were normally distributed after each index was applied. The Shapiro-Wilk Normality test is most reliable with small sample sizes, and accordingly, we computed ten iterations of the Shapiro-Wilk Normality test, each extracting 100 random samples from the 500 kelp samples and 500 water samples from each image acquisition and spectral index (H. Huang et al., 2016).

Table 1. Blue (B), green (G), red (R), red-edge (Re), and NIR band combinations for each of the vegetation indices tested for the separability analysis of kelp and water pixels.

Description	Equation	Reference
Red-Blue	$R - B$	
Normalized Difference of Red and Blue (NDRB)	$\dfrac{R - B}{R + B}$	
Modified Green Red Vegetation Index (MGVI)	$\dfrac{G^2 - R^2}{G^2 + R^2}$	Bendig et al., 2015
Modified Photochemical Reflectance Index (MPRI)	$\dfrac{G - R}{G + R}$	Yang et al., 2008
Red Green Blue Vegetation Index (RGBVI)	$\dfrac{G - B * R}{G^2 + B * R}$	Bendig et al., 2015
Green Leaf Index (GLI)	$\dfrac{2G - R - B}{2G + R + B}$	Louhaichi et al., 2001
Greenness Index (GI)	$\dfrac{G}{R}$	Smith et al., 2005

Blue/Red	$\dfrac{B}{R}$	
Excess of Green (ExG)	$2G - R - B$	Woebbecke et al., 1995
Visible Atmospherically Resistant Index (VARI)	$\dfrac{G - R}{G + R - B}$	Gitelson et al., 2002
Triangular Vegetation Index (TVI)	$\dfrac{120(Re - G) - 200(R - G)}{2}$	Broge & Leblanc, 2001
Normalized Difference Vegetation Index (NDVI)	$\dfrac{NIR - R}{NIR + R}$	Tucker, 1979
Green Normalized Difference Vegetation Index (Green NDVI)	$\dfrac{NIR - G}{NIR + G}$	Gitelson et al., 1996
Normalized Difference Blue Index (Blue NDVI)	$\dfrac{NIR - B}{NIR + B}$	Zerbe & Liew, 2004
Renormalized Difference Vegetation Index (RDVI)	$\dfrac{NIR - R}{\sqrt{NIR + R}}$	Roujean & Breon, 1995
Normalized Difference Red-edge Blue (NDBRE)	$\dfrac{Re - B}{Re + B}$	
Enhanced Vegetation Index (EVI)	$2.5\left[\dfrac{NIR - R}{NIR + 6*R - 7.5*B + 1}\right]$	Huete et al., 2002
Green Chlorophyll Index (CIG)	$\dfrac{NIR}{G} - 1$	Gitelson et al., 2005
Blue/Red-edge	$\dfrac{B}{Re}$	
Blue/NIR	$\dfrac{B}{NIR}$	

In order to identify kelp using a vegetation index, we identified a threshold, and pixels above this threshold were considered kelp canopy. Ideally, we would have used a single threshold for all images, but differing sensors, illumination conditions, and kelp condition necessitated a more dynamic approach. For each image, we calculated histograms from vegetation index values. For images containing both kelp and water, histograms displayed a bimodal signature, with one peak characterizing kelp pixels and the other characterizing water. We identified the location of each histogram peak with the function *findpeaks* in MATLAB 2018a, calculated the mid-point, and used the vegetation index value at the mid-point as the unique, image-based classification threshold (Fig. 3). If we were only able to identify one peak (i.e. the image was dominated by either kelp or water pixels), we applied the function *gradient* in MATLAB 2018a to identify potential shoulders within the histogram. In these images, we used the vegetation index value at the mid-point between the shoulder and the peak as the unique, image-based classification threshold.
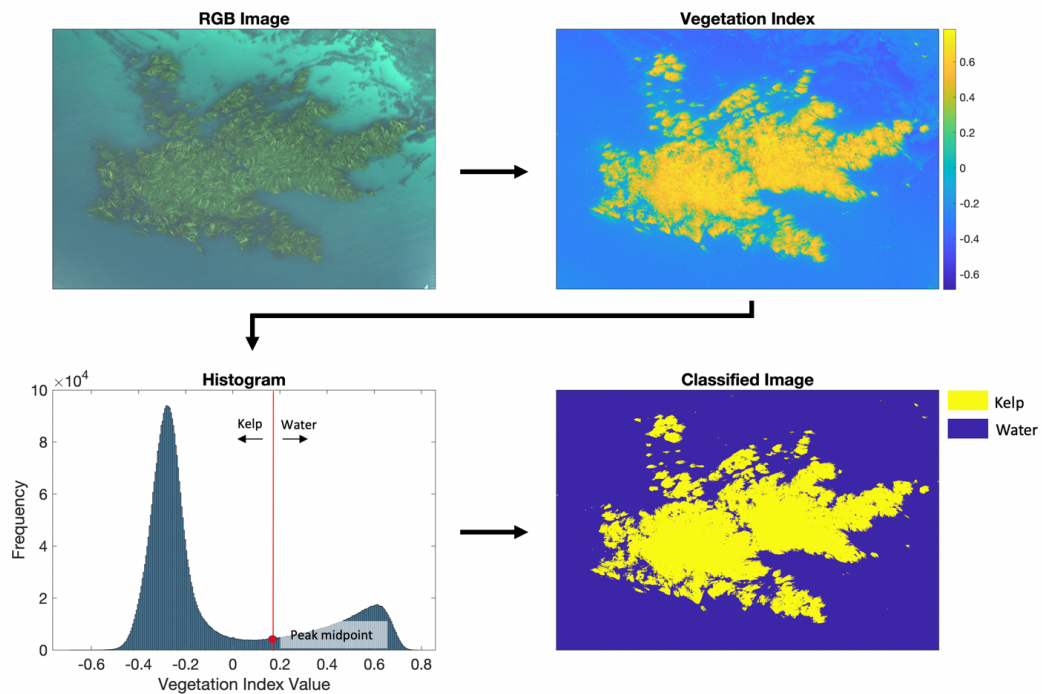

Fig. 3. Methodology used in the detection of the presence or absence of kelp in each pixel. For each image, we applied the vegetation index and calculated histograms to find unique thresholds for image classifications.

11

Using the separability measures, we identified the best performing RGB-based index and the best performing red-edge or NIR-based index (Red-Blue and NDBRE, see Results). We then performed an accuracy assessment to compare the automated classifications from these two indices. Using the same randomly selected 5,000 kelp and water pixels used within the TD and JD separability analysis, we quantified how many pixels each index accurately classified as kelp or water and determined where each index fails.

NDBRE yielded the highest accuracy, and we applied the NDBRE histogram-based automated classification to each image in Honeymoon Cove tidal surveys, Arroyo Quemado tidal surveys, Arroyo Quemado current surveys, and Honeymoon Cove time series. We multiplied the number of kelp pixels in each classified image by the area of each pixel (10 cm x 10 cm) to calculate the amount of kelp canopy present. For the tidal analysis, we compared the identified kelp area from Arroyo Quemado to ADCP tidal measurements from the SBC LTER project and the identified kelp area from Honeymoon Cove to NOAA/NOS/CO-OPS one-minute tidal measurements. We used the station-measured tidal height at the mid-point of each flight for input in a simple linear regression model. For the current analysis, we compared the identified kelp area from Arroyo Quemado to ADCP current measurements from the SBC LTER project taken within the kelp forest at 12.5m (from the bottom).

2.4 Seasonal Variability in Kelp Abundance

We collected biweekly imagery at Honeymoon Cove from June 2018 to August 2019 for a total of 25 images. We conducted all flights at mid-tide (~ 1 m) to reduce the impact of tides on surface canopy measurements. We did not restrict flights due to time of day or cloud coverage, however, we did not fly on days with wind speeds > 16 km/h or in precipitation of any kind.

For qualitative comparisons between seasonal variations in kelp canopy area and

environmental variables, we collected SST measurements from the NOAA National Data Buoy Center Station 9410660 and aggregated the measurements to daily means. Additionally, we collected maximum wave height data from the Coastal Data Information Program's (CDIP) nowcast alongshore wave-propagation model (O'Reilly et al., 2016). The model uses various parameters from sites located at 100 m intervals along the backbeach to calculate hourly estimates of maximum wave height at a depth of 10 m along the California coastline. We selected the five sites that incorporated calculations from the backbeach within Honeymoon Cove (sites L0389 - L0394) and averaged them by date and time. We calculated the daily maximum wave height for analysis.

2.5 Statistical Analyses

Tidal height and current speed are strongly correlated, and as a result, we performed several statistical analyses to detect and separate the effects of tides and currents on variations in kelp canopy area (Britton-Simmons et al., 2008). For each tidal survey (both Honeymoon Cove surveys and the Arroyo Quemado survey), we applied a simple linear regression to determine whether tidal height (independent variable) was significantly correlated with kelp canopy area (dependent variable). To test for potential differences between the Honeymoon Cove tidal surveys due to current speed, we used a one-way analysis of covariance (ANCOVA) to determine whether the Honeymoon Cove simple linear regression slopes from the two tidal survey dates were equal. To test for potential differences in the relationship between tidal height and kelp canopy area at Honeymoon Cove and Arroyo Quemado, we used an ANCOVA to determine if the simple linear regression slopes between the two sites were significantly different from each other.

For the Arroyo Quemado tidal and current surveys, we used multiple linear regression to

determine whether tidal height and current speed (independent variables) were significantly

correlated with kelp area (dependent variable; Britton-Simmons et al., 2008). Additionally, we

calculated partial correlation coefficients to partition the variance in canopy area explained by

tidal height or current speed (Britton-Simmons et al., 2008). Partial correlation coefficients

measure the correlation between two variables while holding a specified covariate constant (i.e.

correlation between tidal height and kelp canopy area while holding current speed constant, and

the correlation between current speed and kelp canopy area while holding tidal height constant;

Sokal & Rohlf 1981).

3. Results

3.1 Kelp and Water Separability Analysis

The twenty vegetation indices yielded variable performances in the parametric

separability analysis of kelp and water pixel samples. P-values from the Shapiro-Wilk Normality

test, which indicate whether the data come from a normally distributed population, varied within

and between the ten iterations performed on each vegetation index. All of the data were not

considered to be normally distributed, which may introduce bias into the JM and TD tests.

However, these results were only used to help inform the optimal vegetation index for analysis.

For the RGB-based vegetation indices, Red-Blue exhibited the highest cumulative JM and TD

values (1.29 and 1.47, respectively), while NDRB exhibited the next highest cumulative values

(1.29 and 1.42, respectively; Fig. 4). None of the RGB-based vegetation indices yielded

completely separable results. For vegetation indices that included either the red-edge or NIR

band, each index exceeded separability scores of 1.5 or greater for both JM and TD. NDBRE

exhibited the highest cumulative JM and TD values (1.99 and 1.99, respectively), while Blue

NDVI exhibited the next highest cumulative values (1.91 and 1.93, respectively; Fig. 5).

Blue/Red-edge was the only vegetation index that yielded a completely separable TD score of 2, while no vegetation index yielded a completely separable JM score (Fig. 4, Fig. 5).

Fig. 4. JM and TD values for the 10 RGB vegetation indices, with 0 being no separability between classes and 2 being complete separability.
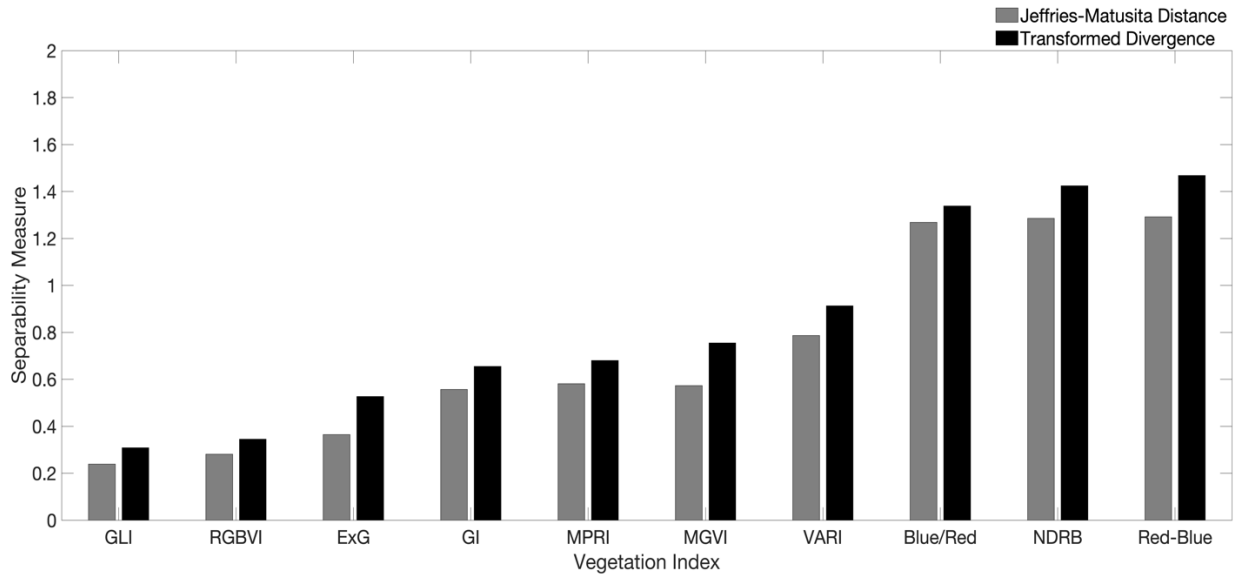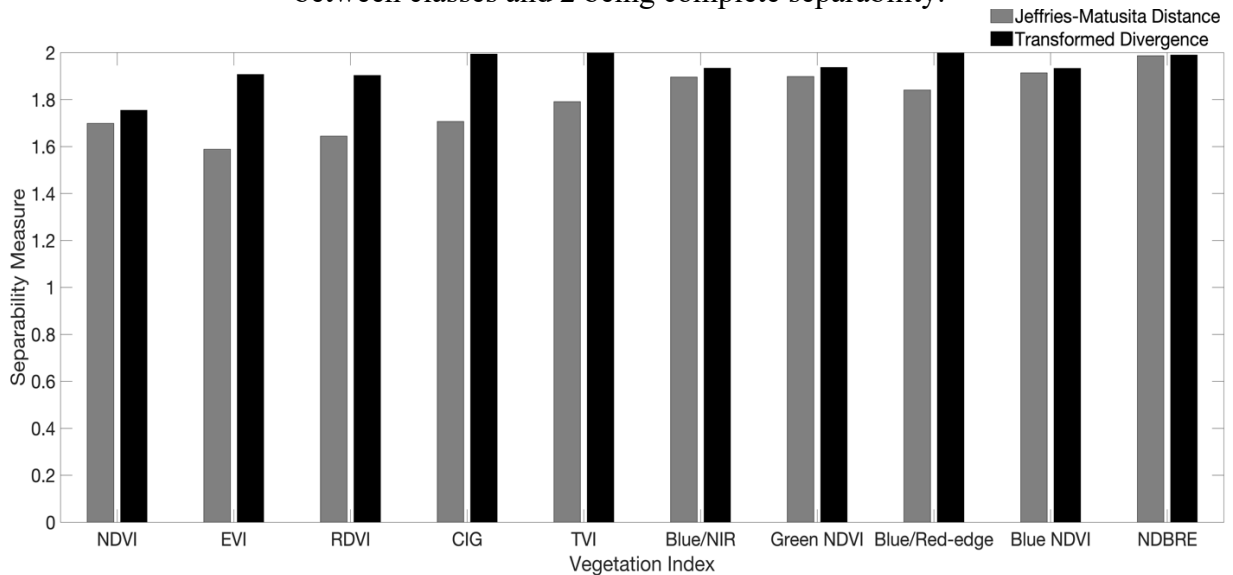

Fig. 5. JM and TD values for the 10 red-edge or NIR-based vegetation indices, with 0 being no separability between classes and 2 being complete separability.

3.2 Automated Classification Accuracy Assessment

The Red-Blue and NDBRE performances in separating kelp and water pixel samples led to further analysis of these vegetation indices for use in the histogram-based automated

classification. Red-Blue exhibited 84.92% accuracy in identification of the randomly selected 5000 pixels used as inputs for the JM and TD separability analysis, and 85.26% accuracy in identification of the randomly selected 5000 water pixels. NDBRE exhibited 98.70% and 99.96% accuracy in identification of kelp and water pixels, respectively. Red-Blue was sensitive to water surface features (ripples and waves), remnant glint artifacts, shadows (i.e. from steeply sloped shoreline), and visible substrate (i.e. on a day with high water clarity), often mis-classifying these features as kelp. Darkly shaded kelp fronds and remnant glint on kelp fronds were often mis-classified as water. NDBRE was much more robust and was able to accurately classify kelp and water pixels across a wide variety of environmental conditions and was used to distinguish kelp from water in all further analyses.

3.3 Tidal Analysis

A simple linear regression showed tidal height was significantly correlated with kelp canopy area in both Honeymoon Cove tidal surveys ($F(1,5) = 213.19$, $p < 0.001$ and $F(1,4) = 10.39$, $p = 0.03$, respectively) and in the Arroyo Quemado tidal survey ($F(1,5) = 134.69$, $p < 0.001$; Fig. 6). Tides had a large impact on the amount of kelp canopy exposed in southern California aerial imagery, as a 1 m increase in tidal height resulted in a 30.26% and 32.30% decrease in kelp canopy area during the first and second Honeymoon Cove tidal surveys, respectively, and a 15.67% decrease in kelp canopy area at the Arroyo Quemado kelp forest (Fig. 6).
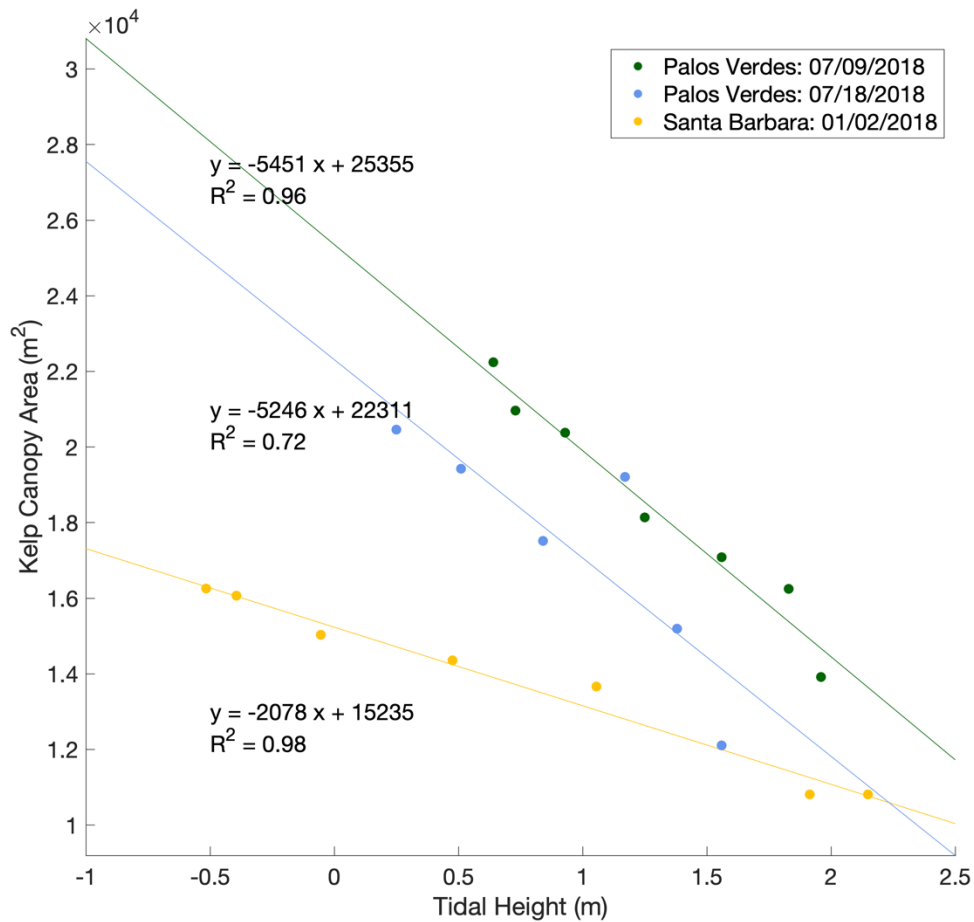
Fig. 6. Regression analysis between kelp canopy area and tidal height for each tidal survey completed at Honeymoon Cove and Arroyo Quemado.

The reduction in canopy area with increasing tidal height was similar between the two Honeymoon Cove tidal surveys, as the slopes of the Honeymoon Cove regression lines (one for each tidal survey date) were not significantly different. $(F_{(1,9)} = 0.02, p = 0.90)$. The reduction in canopy area with increasing tidal height was greater in both Honeymoon Cove surveys than it was at Arroyo Quemado $(F_{(1,10)} = 60.18, p < 0.001$ and $F_{(1,9)} = 6.83, p = 0.02$, respectively).

During the Arroyo Quemado tidal survey, current speeds generally increased as tidal heights reached their minimum (Fig. 7). The multiple regression analysis from the Arroyo Quemado tidal survey showed a significant negative relationship between tidal height and kelp area $(p = 0.01$; Table 2). The relationship between current speed and kelp area was found to be

positive, but was insignificant (p = 0.65; Table 2). The partial correlation analysis showed that if the effects of current speed were controlled, tidal height would have explained 86.90% of the observed variation in and kelp canopy area. By contrast, contribution of current velocity explained only 5.7% of the observed variation in canopy area, and this result was not significant (p = 0.65; Table 2).
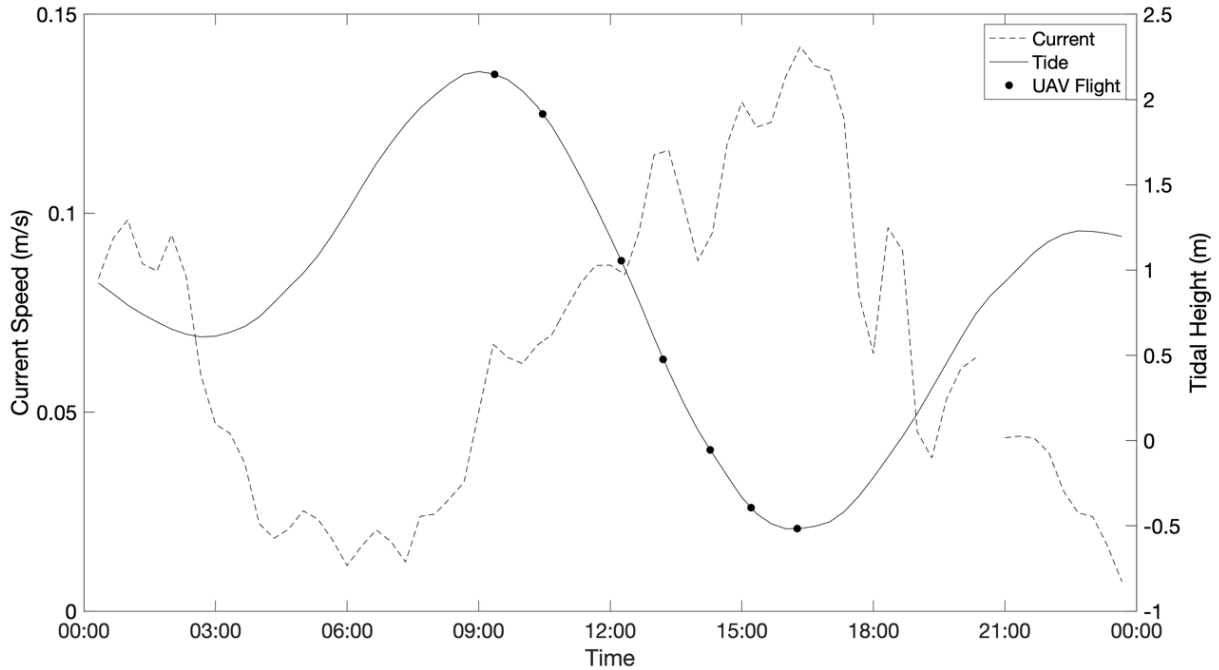
Fig. 7. Temporal variations in tidal height and current speed during each flight of the Arroyo Quemado tidal survey.

Table 2. Multiple regression and partial correlation analysis results from the Arroyo Quemado tidal survey. * indicates statistical significance.

| Multiple Regression Analysis | | | | Partial Correlation Analysis | | | |
| Coefficients | | | | Tide Effect | | Current Effect | |
Intercept	Tide	Current	R^2	r	R^2	r	R^2
14441.5*	-1913.3*	6912.3	0.98	-0.932*	0.869	0.238	0.057

3.4 Current Analysis

Current speeds ranged from 0.02 to 0.13 m/s across the five dates, which was representative of average conditions in the Arroyo Quemado kelp forest during 2019 as a whole

(Fig. 9; annual average of 0.085 ± 0.066 m/s). Current speed exhibited a negative linear relationship with kelp canopy area but was not significantly correlated with the amount of kelp canopy exposed during the Arroyo Quemado current survey ($F_{(1,5)} = 6.05$, $p = 0.09$; Fig. 8). However, canopy area declined by 31.99% percent for a 0.1 m/s increase in current velocity.
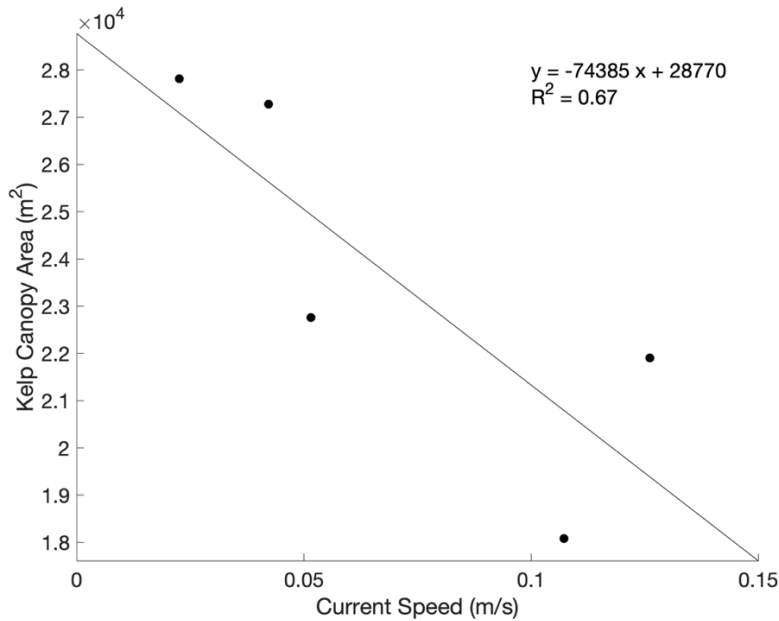
Fig. 8. Regression analysis between kelp canopy area and current speed during the Arroyo Quemado current surveys.

During the Arroyo Quemado current survey, there was no consistent relationship between tidal height and current speed (Fig. 9) and the two were not significantly correlated ($F_{(1,5)} = 1.92$, $p = 0.23$). The multiple regression analysis from the Arroyo Quemado current survey showed neither a significant effect of current speed on kelp area, nor a significant effect of tidal height ($F_{(2,5)} = 2.01$, $p = 0.33$). The partial correlation analysis showed that neither tidal height nor current speed accounted for statistically significant kelp area variation. With the effects of tidal height controlled, variability in current speed accounted for 73.75% of the variability in kelp area during the current survey ($p = 0.26$). Tidal height only explained 2.72% of the variability in kelp area during the survey ($p = 0.97$).
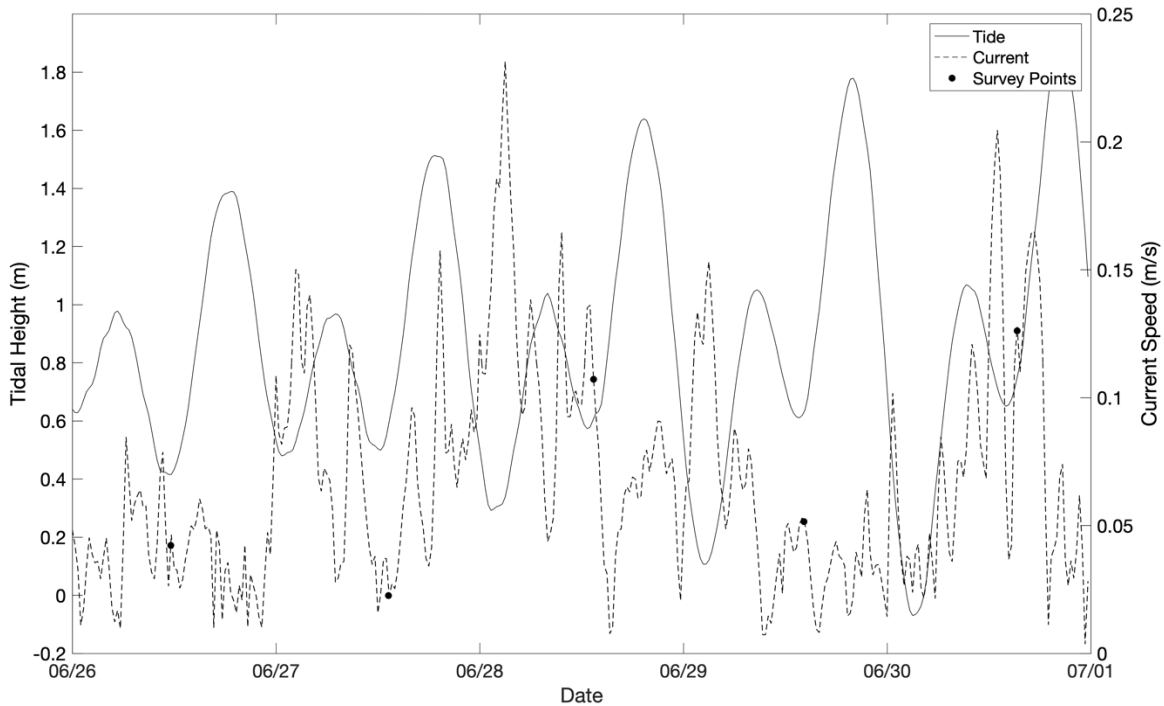
Figure 9. Temporal variations in tidal height and current speed during each flight of the Arroyo Quemado current survey.

3.5 Honeymoon Cove Time Series

The mean kelp canopy area across the time series (June 2018 to August 2019) was 6763.2 m², but there was a high amount of variability about this mean. With a standard deviation of 7104.6 m², the coefficient of variation across the 25 surveys was 1.05. Changes in kelp canopy area occurred over a seasonal cycle with kelp area maximums in late summer and minimums in winter (Fig. 10). There was also pronounced seasonal variability, as mortality and growth each progressed for about four months (from late summer to fall and from spring to early summer, respectively) before reaching maximum or minimum values (Fig. 10). These gradual changes coincided with SST patterns, with kelp declines occurring after warmer periods and growth occurring after cooler periods (Fig. 10). Rapid changes also occurred within seasonal time spans, as evidenced by kelp recovery in November, which was followed by dislodgement from large

wave events in December. Low kelp canopy area persisted until wave events subsided in late

spring (Fig. 10).
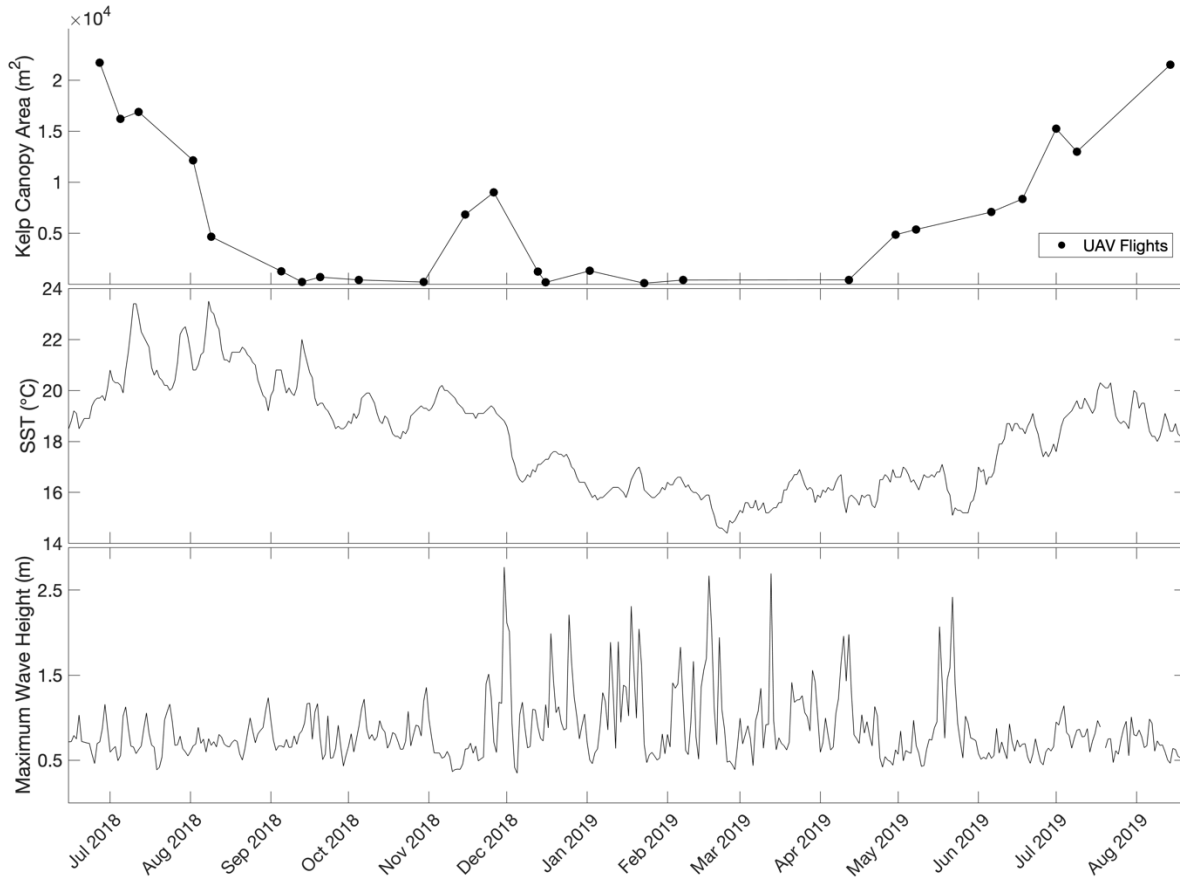
Figure 10. Honeymoon Cove UAV-derived time series of kelp canopy area from June 2018 to
August 2019.

4. Discussion

4.1 UAV Data Collection, Processing, and Classification

Our automated method for detecting kelp canopy can be applied to both multispectral and

RGB UAV imagery and is highly accurate across a range of weather, ocean, and illumination

conditions. This robustness is important as there are a number of challenges associated with

UAV-based remote sensing in coastal zones (Bevan et al., 2016; Hodgson et al., 2013; Schaub et

al., 2018). Weather conditions, including precipitation and high wind, are common limiting

21

factors in drone deployment. Sun can also be a limiting factor for marine applications, as glint features on the water surface are challenging for photogrammetric software packages to manage. During stitching, the software may use glint artifacts as tie points to stitch two non-neighboring images in error, or it may be unable to find tie points altogether due to the lack of viable pixels. Additionally, any remaining glint in orthomosaics can introduce spectral noise and bias classification efforts. Sun glint can be reduced or avoided by collecting data on overcast days or by flying when the sun is at lower angles in the sky, but this is not always possible as flights may need to be conducted at a certain tidal stage. By introducing sun glint masks into our image processing workflow, PhotoScan alignment success increased in almost every flight and the presence of sun glint greatly decreased in final orthomosaics.

Another challenge of using UAV imagery for analysis in marine ecosystems includes changing illumination conditions within flights (i.e. on a partly cloudy day when the sun continuously emerges and disappears behind clouds) and between flights (i.e. flying on an overcast day and flying on a sunny day). Despite spectral corrections with reflectance panels, these variations impact output reflectance values and cause spectral inconsistencies. As a result, using supervised classification schemes to distinguish kelp from water is difficult, as the training data often does not adequately cover the spectral ranges observed through each flight (Taddia & Russo, 2019). Additionally, while vegetation indices help to distinguish kelp from water, the threshold for separation strongly depends on image-specific spectral values, in turn necessitating image-specific thresholds (Taddia & Russo, 2019). Our dynamic thresholding procedure for color and multispectral UAV imagery removed the subjectivity and visual bias involved with manual threshold selection and was highly accurate (over 84% and 98%, respectively) in classifying exemplary kelp and water pixels. However, it is important to note that this accuracy was determined using ideal kelp and water samples, and the overall accuracy of the classified

image may be lower.

Our highest accuracies were achieved using multispectral imagery, and a number of other studies have demonstrated the utility of multispectral imagery in detecting kelp canopy (Cavanaugh et al., 2010; Jensen et al., 1980). While many traditional floating algae indices depend on the NIR band (Cavanaugh et al., 2010; Hu, 2009; Tucker, 1979; Xing & Hu, 2016), the NIR band on the RedEdge has higher variability as compared to field spectra, which may have led to slightly lower separability potential from NIR-based indices (Doughty & Cavanaugh, 2019). We also found that accuracies of > 80% could be achieved using RGB imagery using a simple subtraction between the red and the blue band. This indicates potential for kelp mapping using accessible low-cost UAV platforms that come with digital cameras. However, users should be aware that RGB imagery is more sensitive to surface features (ripples and waves), remnant glint artifacts, shadows (i.e. from steeply sloped shoreline), and visible substrate (i.e. on a day with high water clarity).

4.2 Effects of Tidal Height and Current Speed on Exposed Canopy

The amount of kelp canopy visible on the water surface at both Honeymoon Cove and Arroyo Quemado declined significantly with tidal height, suggesting that tides have the ability to bias aerial-derived metrics of kelp canopy coverage in southern California. The effect of tide was not consistent between the two sites and was almost twice as strong at Honeymoon Cove, which may be the result of differing bed structures between the two sites. The Arroyo Quemado kelp forest is comprised of a discrete, offshore bed, while the Honeymoon Cove kelp forest is comprised of both large, dense kelp stands as well as small, sparse stands. At Arroyo Quemado, the depth linearly slopes downward from the shoreline (from about -1.5 m to -16.5m), but the extensive rocky reef along the gradient allows for a continuous, dense canopy. Increases in tidal

height submerged the edges of the canopy but did not submerge any central canopy features. At Honeymoon Cove, the depth slopes downward from the outer edges of the cove to the center (from about 0 m to -8 m). There is extensive and continuous rocky reef along the shallow, edges of the cove, but the reef in the center is much more fragmented. As a result, dense aggregates of kelp grow along edges, and these behave similarly to the beds at Arroyo Quemado as tidal height increases. However, the patchy, fragmented aggregates in the center of the cove often only consist of a few individuals, and these become fully submerged as the tide increases (Fig. 1). Kelp forest demographics might also influence the impacts of tides by controlling the fraction of canopy vs. subsurface fronds.

A region's tidal range will clearly influence the degree to which UAV estimates of canopy area are affected by tides. Southern California has a generally low tidal range (~ 2 m) compared to some other global regions (i.e. Southeast Alaska, ~ 30 m). Yet, even this small range impacted kelp canopy coverage by over 15% at Arroyo Quemado and over 30% at Honeymoon Cove. This result disagrees with previous work that estimated the weak tidal fluctuations in Santa Barbara had no effect on kelp canopy coverage estimates from Landsat satellite imagery (Cavanaugh et al., 2010, 2011). However, the higher resolution of the UAV imagery and experimental design aimed at isolating the effects of tides likely enabled us to more clearly detect the tidal effect. Another study using Landsat imagery for kelp canopy detection found inconsistencies in kelp biomass estimates between Landsat TM and ETM+ sensors, which was attributed to the 8-day repeat difference between the satellites imaging at different points in the tidal cycle (Bell et al., 2020). Aggregating Landsat biomass estimates (30 m resolution) to a seasonal scale (3 months) was sufficient for correcting for tidal effects (Bell et al., 2020).

Tidal height explained 87% of the variation in kelp canopy area during the Arroyo Quemado tidal survey, which is consistent with findings from other regions with similar tidal

signals, such as San Juan Island, WA (Britton-Simmons et al., 2008). Kelp beds adjacent to San Juan Island experience tidal ranges of 2 to 3 m and are mainly comprised of bull kelp (*Nereocystis luetkeana*). Britton-Simmons et al. (2008) found that tidal height explained between 67% and 95% of observed variability in kelp area across 6 different sites near San Juan Island, which included differing kelp densities, bathymetry, coastline shapes, and current strength. While both giant kelp and bull kelp form floating canopies, they exhibit unique morphological features. Each giant kelp blade is attached to a pneumatocyst that buoys it to the surface (Graham et al., 2007), while bull kelp blades for one individual grow from a single, large (15 cm diameter) pneumatocyst (Amsler & Neushul, 1989; Schroeder et al., 2019). As a result, giant kelp canopies consist of stipes, pneumatocysts, and blades, while bull kelp canopies mainly consist of stipes and pneumatocysts; bull kelp fronds often remain submerged (Schroeder et al., 2019). While these morphological differences responded similarly to tidal fluctuations in southern California and San Juan Island, they may exhibit different effects in regions with more extreme tidal fluctuations.

Currents had no apparent effect on the amount of kelp canopy visible on the water surface, as canopy area was not significantly correlated with current speed. However, the relationship may have been significant if more samples were included in the study. Current speeds at Arroyo Quemado never exceeded 0.13 m/s during our survey, and while the correlation between kelp canopy area and current speed was not significant, a 0.1 m/s increase in current speed reduced the amount of floating canopy by over 30%. Our results agree with previous studies that found no correlation between current speed and observed canopy area of bull kelp in regions with low current speeds (Britton-Simmons et al., 2008). Britton-Simmons et al. (2008) found that in 1 of the 6 beds from the San Juan Island study, current speeds never exceeded 0.4 m/s. In this bed, there was no clear trend in the relationship between current speed and the

amount of visible kelp on the water surface (n > 20; Britton-Simmons et al., 2008). In contrast, the trend between current speed and the amount of visible kelp on the water surface at Arroyo Quemado, although not significant, was linear, but additional sampling is needed to understand whether this relationship is significant and consistent across higher current speeds.

The effects of current speed on the other 5 kelp beds from Britton-Simmons et al. (2008) were found to be highly significant, but current speeds ranged much higher at these sites (> 1 m/s). While low current speeds may impact giant kelp and bull kelp similarly, the relationship may change as current speed increases. Bull kelp blades begin to stream laterally with moderate amounts of current, resulting in larger floating canopies. As a result, the relationship between the percentage of bull kelp bed visible and current speed is often non-linear and difficult to quantify, as it varies with geographic shading, coastline shape, and bathymetry (Britton-Simmons et al., 2008). The spatial variation in current dynamics around kelp beds is extremely dynamic, and necessitates site-specific corrections – especially in places with high current ranges (Britton-Simmons et al., 2008). However, our results support that despite the relatively weak current patterns at Arroyo Quemado, current speeds at the higher end of the current range at Arroyo Quemado can bias canopy estimates.

4.3 UAV Kelp Canopy Time Series

Our UAV time series dataset represents a high-resolution assessment of local kelp canopy area dynamics on a sub-seasonal scale. Previous studies have demonstrated the effectiveness of deriving time series of kelp canopy biomass or area from aerial and satellite imagery, but many of these analyze data on quarterly or annual time scales (Bell et al., 2020; Bell, Cavanaugh, & Siegel, 2015; Berry et al., 2005; Cavanaugh et al., 2010, 2011, 2019; Deysher, 1993; Jensen et al., 1980; Pfister et al., 2018; Rogers-Bennett & Catton, 2019; Schroeder et al., 2019; Stekoll et

al., 2007). This UAV dataset provides a novel view into the feasibility for collecting long-term datasets at high spatial and temporal resolution, and the potential for understanding the rapid, sub-seasonal variations in canopy dynamics.

We conducted flights for our area of interest using one battery set (20 to 30-minute flights), allowing for feasible and relatively quick bi-weekly data collection. Additionally, mostly automated processing workflows (reflectance corrections, PhotoScan workflow, and classifications) allowed for dataset manageability, as processing took about 5 hours from start to finish (about 4.5 hours were automated). This time would decrease with more computing power and/or GPU processing.

The Honeymoon Cove time series displayed intra-annual variability that are typical of giant kelp. Increased temperature and decreased nutrients in the late summer were associated with gradual declines in kelp coverage. The first large wave event of the winter yielded immediate kelp declines, and abundance remained low until wave events began to subside in the spring. As temperature and nutrient conditions became adequate, kelp abundance continued to increase until reaching a peak in late summer. However, we were also able to capture fine-scale changes in kelp canopy area that would have gone undetected in an annual or quarterly dataset. Kelp cover increased to about half of its maximum in the late fall before wave events began (Fig. 10). This increase may have been linked to increased nutrient levels, as it occurred as temperatures decreased and began to approach winter minimums. However, a number of other factors may have been involved, including increased light availability and unoccupied substrate following the late fall kelp decline.

5. CONCLUSION

The spatial and temporal capabilities of UAV imagery make these platforms useful for

local mapping of giant kelp canopies at high spatial resolution. Collecting repeated measurements of kelp canopy area is difficult at a relatively small spatial scales (e.g. less than a few square meters), as diving efforts require extensive data collection, photographs taken at water level are difficult to quantify, and estimates from most satellite platforms do not provide suitable resolutions (Britton-Simmons et al., 2008; D. Reed et al., 2009; D. C. Reed et al., 2008; Schroeder et al., 2019). UAVs were an ideal platform for quantifying the effect of tides and currents on the amount of floating kelp canopy in southern California. Tidal height and current speed both introduced bias to canopy estimates, but the magnitude of their impacts was dependent upon several factors, including differing kelp densities, species type, bathymetry, coastline shapes, and current strengths, making them region specific.

As a powerful monitoring tool, UAVs were also used to map kelp in small, sparse beds close to the coast, to create high spatial resolution time series, and to examine the impacts of discrete disturbances such as large wave events. However, this high spatial resolution comes at the expense of the broad spatial coverage of satellites, and neither method can robustly replace the other. The choice of which method to use is highly dependent on the ecological questions being asked.

References

Amsler, C. D., & Neushul, M. (1989). Diel periodicity of spore release from the kelp *Nereocystis Luetkeana*. *J. Exp. Mar. Biol. Ecol*, *134*, 117–127.

Bell, T. W., Allen, J. G., Cavanaugh, K. C., & Siegel, D. A. (2020). Three decades of variability in California's giant kelp forests from the Landsat satellites. *Remote Sensing of Environment*, *238*(June 2018), 110811. https://doi.org/10.1016/j.rse.2018.06.039

Bell, T. W., Cavanaugh, K. C., Reed, D. C., & Siegel, D. A. (2015). Geographical variability in the controls of giant kelp biomass dynamics. *Journal of Biogeography*, *42*(10), 2010–2021. https://doi.org/10.1111/jbi.12550

Bell, T. W., Cavanaugh, K. C., & Siegel, D. A. (2015). Remote Sensing of Environment Remote monitoring of giant kelp biomass and physiological condition : An evaluation of the potential for the Hyperspectral Infrared Imager (HyspIRI) mission. *Remote Sensing of Environment*, *167*, 218–228. https://doi.org/10.1016/j.rse.2015.05.003

Bendig, J., Yu, K., Aasen, H., Bolten, A., Bennertz, S., Broscheit, J., Gnyp, M. L., & Bareth, G. (2015). Combining UAV-based plant height from crop surface models, visible, and near infrared vegetation indices for biomass monitoring in barley. *International Journal of Applied Earth Observation and Geoinformation*, *39*, 79–87. https://doi.org/10.1016/j.jag.2015.02.012

Berry, H. D., Mumford, T. F., & Dowty, P. (2005). *Using Historical Data to Estimate Changes in Floating Kelp (Nereocystis luetkeana and Macrocystis integrifolia) in Puget Sound, Washington*. *Berry 2001*, 1–6. http://depts.washington.edu/uwconf/2005psgb/2005proceedings/papers/F7_BERRY.pdf%0Apapers3://publication/uuid/A9C39740-8651-46F0-A52A-D1E89664AF5C

Bevan, E., Wibbels, T., & Najera, B. M. Z. (2016). Using Unmanned Aerial Vehicle (UAV) Technology for Locating, Identifying, and Monitoring Courtship and Mating Behavior in the Green Turtle (Chelonia mydas) TECHNIQUES TECHNIQUES. *TECHNIQUES 27 Herpetological Review*, *47*(1), 27–32.

Britton-Simmons, K., Eckman, J. E., & Duggins, D. O. (2008). Effect of tidal currents and tidal stage on estimates of bed size in the kelp Nereocystis luetkeana. *Marine Ecology Progress Series*, *355*, 95–105. https://doi.org/10.3354/meps07209

Broge, N. H., & Leblanc, E. (2001). Comparing prediction power and stability of broadband and hyperspectral vegetation indices for estimation of green leaf area index and canopy chlorophyll density. *Remote Sensing of Environment*, *76*(2), 156–172. https://doi.org/10.1016/S0034-4257(00)00197-8

Castorani, M. C. N., Reed, D. C., Alberto, F., Bell, T. W., Simons, R. D., Cavanaugh, K. C., Siegel, D. A., & Raimondi, P. T. (2015). Connectivity structures local population dynamics: A long-term empirical test in a large metapopulation system. *Ecology*, *96*(12), 3141–3152. https://doi.org/10.1890/15-0283.1

Castorani, M. C. N., Reed, D. C., Raimondi, P. T., Alberto, F., Bell, T. W., Cavanaugh, K. C., Siegel, D. A., & Simons, R. D. (2017). Fluctuations in population fecundity drive variation in demographic connectivity and metapopulation dynamics. *Proceedings of the Royal Society B: Biological Sciences*, *284*(1847). https://doi.org/10.1098/rspb.2016.2086

Cavanaugh, K. C., Kendall, B. E., Siegel, D. A., Reed, D. C., Alberto, F., & Assis, J. (2013). Synchrony in dynamics of giant kelp forests is driven by both local recruitment and regional environmental controls. *Ecology*, *94*(2), 499–509. https://doi.org/10.1890/12-0268.1

Cavanaugh, K. C., Reed, D. C., Bell, T. W., Castorani, M. C. N., Beas-luna, R., & Barrett, N. S. (2019). *Spatial Variability in the Resistance and Resilience of Giant Kelp in Southern and Baja California to a Multiyear Heatwave*. *6*(July), 1–14. https://doi.org/10.3389/fmars.2019.00413

Cavanaugh, K. C., Siegel, D. A., Kinlan, B. P., & Reed, D. C. (2010). Scaling giant kelp field measurements to regional scales using satellite observations. *Marine Ecology Progress Series*, *403*, 13–27. https://doi.org/10.3354/meps08467

Cavanaugh, K. C., Siegel, D. A., Raimondi, P. T., & Alberto, F. (2014). Patch definition in metapopulation analysis: A graph theory approach to solve the mega-patch problem. *Ecology*, *95*(2), 316–328. https://doi.org/10.1890/13-0221.1

Cavanaugh, K. C., Siegel, D. A., Reed, D. C., & Dennison, P. E. (2011). Environmental controls of giant-kelp biomass in the Santa Barbara Channel, California. *Marine Ecology Progress Series*, *429*, 1–17. https://doi.org/10.3354/meps09141

Changhui, Y., Yuan, Y., Minjing, M., & Menglu, Z. (2013). Cloud Detection Method Based on Feature Extraction in Remote Sensing Images. *International Archives of the Photogrammetry, Remote Sensing and Spatial Information Sciences*, *XL-2/W1*(2013 8th International Symposium on Spatial Data Quality), 173–177.

Deysher, L. E. (1993). Evaluation of remote sensing techniques for monitoring giant kelp populations. *Hydrobiologia*, *260–261*(1), 307–312. https://doi.org/10.1007/BF00049033

Doughty, C., & Cavanaugh, K. (2019). Mapping Coastal Wetland Biomass from High Resolution Unmanned Aerial Vehicle (UAV) Imagery. *Remote Sensing*, *11*(5), 540. https://doi.org/10.3390/rs11050540

Dugan, J. E., Hubbard, D. M., Mccrary, M. D., & Pierson, M. O. (2003). *The response of macrofauna communities and shorebirds to macrophyte wrack subsidies on exposed sandy beaches of southern California*. 25–40. https://doi.org/10.1016/S0272-7714(03)00045-3

Gentry, R. R., Alleway, H. K., Bishop, M. J., Gillies, C. L., Waters, T., & Jones, R. (2019). Exploring the potential for marine aquaculture to contribute to ecosystem services. *Reviews in Aquaculture*, 499–512. https://doi.org/10.1111/raq.12328

Gentry, R. R., Froehlich, H. E., Grimm, D., Kareiva, P., Parke, M., Rust, M., Gaines, S. D., & Halpern, B. S. (2017). Mapping the global potential for marine aquaculture. *Nature Ecology*

and Evolution, *1*(9), 1317–1324. https://doi.org/10.1038/s41559-017-0257-9

Gitelson, A. A., Kaufman, Y. J., & Merzlyak, M. N. (1996). Use of a green channel in remote sensing of global vegetation from EOS- MODIS. *Remote Sensing of Environment*, *58*(3), 289–298. https://doi.org/10.1016/S0034-4257(96)00072-7

Gitelson, A. A., Stark, R., Rundquist, D., Gitelson, A. A., Kaufman, Y. J., Stark, R., & Rundquist, D. (2002). *DigitalCommons @ University of Nebraska - Lincoln Novel Algorithms for Remote Estimation of Vegetation Fraction*.

Gitelson, A. A., Viña, A., Ciganda, V., Rundquist, D. C., & Arkebauer, T. J. (2005). Remote estimation of canopy chlorophyll content in crops. *Geophysical Research Letters*, *32*(8), 1–4. https://doi.org/10.1029/2005GL022688

Graham, M. H., Vásquez, J. A., & Buschmann, A. H. (2007). Global Ecology of the Giant Kelp Macrocystis : From Ecotypes To Ecosystems. *Oceanography and Marine Biology*, *45*(January), 39–88. https://doi.org/10.1201/9781420050943.ch2

Hakala, T., Markelin, L., Id, E. H., Scott, B., Theocharous, T., Id, O. N., Näsi, R., Suomalainen, J., Id, N. V., & Greenwell, C. (2018). *Direct Reflectance Measurements from Drones : Sensor Absolute Radiometric Calibration and System Tests for Forest Reflectance Characterization*. https://doi.org/10.3390/s18051417

Hamilton, S. L., Bell, T. W., Watson, J. R., Grorud-Colvert, K. A., & Menge, B. A. (2020). Remote sensing: generation of long-term kelp bed data sets for evaluation of impacts of climatic variation. *Ecology*, *0*(0), 1–13. https://doi.org/10.1002/ecy.3031

Haralick, R. M., Shanmugam, K., & Dinstein, I. (1973). Textural Features for Image Classification. *IEEE Transactions on Systems, Man and Cybernetics*, *SMC-3*(6), 610–621.

Harley, C. D. G., Hughes, A. R., Hultgren, K. M., Miner, B. G., Sorte, C. J. B., Thornber, C. S., Rodriguez, L. F., Tomanek, L., & Williams, S. L. (2006). The impacts of climate change in coastal marine systems. *Ecology Letters*, *9*(2), 228–241. https://doi.org/10.1111/j.1461-0248.2005.00871.x

Hodgson, A., Kelly, N., & Peel, D. (2013). Unmanned aerial vehicles (UAVs) for surveying Marine Fauna: A dugong case study. *PLoS ONE*, *8*(11), 1–15. https://doi.org/10.1371/journal.pone.0079556

Hu, C. (2009). A novel ocean color index to detect floating algae in the global oceans. *Remote Sensing of Environment*, *113*(10), 2118–2129. https://doi.org/10.1016/j.rse.2009.05.012

Huang, H., Roy, D. P., Boschetti, L., Zhang, H. K., Yan, L., Kumar, S. S., Gomez-Dans, J., & Li, J. (2016). Separability analysis of Sentinel-2A Multi-Spectral Instrument (MSI) data for burned area discrimination. *Remote Sensing*. https://doi.org/10.3390/rs8100873

Huang, X., Liu, X., & Zhang, L. (2014). *A Multichannel Gray Level Co-Occurrence Matrix for Multi/Hyperspectral Image Texture Representation*. 8424–8445.

https://doi.org/10.3390/rs6098424

Huete, A., Didan, K., Miura, T., Rodriguez, E. P., Gao, X., & Ferreira, L. G. (2002). Overview of the radiometric and biophysical performance of the MODIS vegetation indices. *Remote Sensing*, *83*, 195–213. https://doi.org/10.1080/0965156x.2013.836857

Jensen, J. R., Estes, J. E., & Tinney, L. (1980). Remote sensing techniques for kelp surveys. *Photogrammetric Engineering & Remote Sensing*, *46*(6), 743–755.

Kellaris, A., Badia, I. M., Gil, A., Neto, A., & Amaral, R. (2019). *Using low - cost drones to monitor heterogeneous submerged seaweed habitats : A case study in the Azores*. *September 2018*, 1909–1922. https://doi.org/10.1002/aqc.3189

Louhaichi, M., Borman, M. M., & Johnson, D. E. (2001). Spatially located platform and aerial photography for documentation of grazing impacts on wheat. *Geocarto International*, *16*(1), 65–70. https://doi.org/10.1080/10106040108542184

Miller, R. J., Lafferty, K. D., Lamy, T., Kui, L., Rassweiler, A., Reed, D. C., & Miller, R. J. (2018). *Giant kelp , Macrocystis pyrifera , increases faunal diversity through physical engineering*.

Mora-Soto, A., Palacios, M., Macaya, E. C., Gómez, I., Huovinen, P., Pérez-Matus, A., Young, M., Golding, N., Toro, M., Yaqub, M., & Macias-Fauria, M. (2020). *A High-Resolution Global Map of Giant Kelp (Macrocystis pyrifera) Forests and Intertidal Green*. 1–20.

Nijland, W., Reshitnyk, L., & Rubidge, E. (2019). Satellite remote sensing of canopy-forming kelp on a complex coastline: A novel procedure using the Landsat image archive. *Remote Sensing of Environment*, *220*, 41–50. https://doi.org/10.1016/j.rse.2018.10.032

O'Reilly, W. C., Olfe, C. B., Thomas, J., Seymour, R. J., & Guza, R. T. (2016). The California coastal wave monitoring and prediction system. *Coastal Engineering*, *116*, 118–132. https://doi.org/10.1016/j.coastaleng.2016.06.005

Pfister, C. A., Berry, H. D., & Mumford, T. (2018). The dynamics of Kelp Forests in the Northeast Pacific Ocean and the relationship with environmental drivers. *Journal of Ecology*, *106*(4), 1520–1533. https://doi.org/10.1111/1365-2745.12908

Reed, D. C., Rassweiler, A., & Arkema, K. K. (2008). Biomass rather than growth rate determines variation in net primary production by giant kelp. *Ecology*, *89*(9), 2493–2505. https://doi.org/10.1890/07-1106.1

Reed, D., Rassweiler, A., & Arkema, K. (2009). Density derived estimates of standing crop and net primary production in the giant kelp Macrocystis pyrifera. *Marine Biology*, *156*(10), 2077–2083. https://doi.org/10.1007/s00227-009-1238-6

Rogers-Bennett, L., & Catton, C. A. (2019). *Marine heat wave and multiple stressors tip bull kelp forest to sea urchin barrens*. 1–9. https://doi.org/10.1038/s41598-019-51114-y

Roujean, J. L., & Breon, F. M. (1995). Estimating PAR absorbed by vegetation from bidirectional reflectance measurements. *Remote Sensing of Environment*, *51*(3), 375–384. https://doi.org/10.1016/0034-4257(94)00114-3

Schaub, J., Hunt, B. P. V., Pakhomov, E. A., Holmes, K., Lu, Y., & Quayle, L. (2018). Using unmanned aerial vehicles (UAVs) to measure jellyfish aggregations. *Marine Ecology Progress Series*, *591*(January), 29–36. https://doi.org/10.3354/meps12414

Schroeder, S. B., Dupont, C., Boyer, L., Juanes, F., & Costa, M. (2019). Passive remote sensing technology for mapping bull kelp (Nereocystis luetkeana): A review of techniques and regional case study. *Global Ecology and Conservation*, *19*, e00683. https://doi.org/10.1016/j.gecco.2019.e00683

Stekoll, M. S., Deysher, L. E., & Hess, M. (2006). A remote sensing approach to estimating harvestable kelp biomass. *Journal of Applied Phycology*, *18*(3–5), 323–334. https://doi.org/10.1007/s10811-006-9029-7

Stekoll, M. S., Deysher, L. E., & Hess, M. (2007). Eighteenth International Seaweed Symposium. *Eighteenth International Seaweed Symposium*, *May 2014*. https://doi.org/10.1007/978-1-4020-5670-3

Taddia, Y., & Russo, P. (2019). *Multispectral UAV monitoring of submerged seaweed in shallow water*.

Thomsen, M. S., Mondardini, L., Alestra, T., Gerrity, S., Tait, L., South, P. M., Lilley, S. A., Schiel, D. R., & Marzinelli, E. M. (2019). *Local Extinction of Bull Kelp (Durvillaea spp .) Due to a Marine Heatwave*. *6*(March), 1–10. https://doi.org/10.3389/fmars.2019.00084

Tucker, C. J. (1979). Red and photographic infrared linear combinations for monitoring vegetation. *Remote Sensing of Environment*, *8*(2), 127–150. https://doi.org/10.1016/0034-4257(79)90013-0

Whitehead, K., & Hugenholtz, C. H. (2014). Remote sensing of the environment with small unmanned aircraft systems (UASs), part 1: a review of progress and challenges. *Journal of Unmanned Vehicle Systems*, *02*(03), 69–85. https://doi.org/10.1139/juvs-2014-0006

Whitehead, K., Hugenholtz, C. H., Myshak, S., Brown, O., LeClair, A., Tamminga, A., Barchyn, T. E., Moorman, B., & Eaton, B. (2014). Remote sensing of the environment with small unmanned aircraft systems (UASs), part 2: scientific and commercial applications. *Journal of Unmanned Vehicle Systems*, *02*, 86–102. https://doi.org/10.1139/juvs-2014-0006

Woebbecke, D. M., Meyer, G. E., Von Bargen, K., & Mortensen, D. A. (1995). Shape features for identifying young weeds using image analysis. *Transactions of the American Society of Agricultural Engineers*, *38*(1), 271–281. https://doi.org/10.13031/2013.27839

Xing, Q., & Hu, C. (2016). Mapping macroalgal blooms in the Yellow Sea and East China Sea using HJ-1 and Landsat data: Application of a virtual baseline reflectance height technique. *Remote Sensing of Environment*, *178*, 113–126. https://doi.org/10.1016/j.rse.2016.02.065

Yang, Z., Willis, P., & Mueller, R. (2008). Impact of Band-Ratio Enhanced Awifs Image To Crop Classification Accuracy. *Pecora 17 – The Future of Land Imaging…Going Operational*, 11.

Zerbe, L. M., & Liew, S. C. (2004). Reevaluating the traditional maximum NDVI compositing methodology: The Normalized Difference Blue Index. *International Geoscience and Remote Sensing Symposium (IGARSS)*, *4*(c), 2401–2404. https://doi.org/10.1109/igarss.2004.1369774

Zheng, G., Li, X., Member, S., Zhou, L., Yang, J., Ren, L., Chen, P., Zhang, H., & Lou, X. (2018). Development of a Gray-Level Co-Occurrence Matrix-Based Texture Orientation Estimation Method and Its Application in Sea Surface Wind Direction Retrieval From SAR Imagery. *IEEE Transactions on Geoscience and Remote Sensing*, *56*(9), 5244–5260. https://doi.org/10.1109/TGRS.2018.2812778